Exploring the Role of Type-II Residual Stresses in a Laser Powder Bed Fusion Nickel-Based Superalloy using Measurement and Modeling

Wesley A. Tayon[1], Darren C. Pagan[2], Saikumar R. Yeratapally[3],

Thien Q. Phan[4], Jacob D. Hochhalter[5]

[1] NASA Langley Research Center, Hampton, VA, 23681

[2] Pennsylvania State University, University Park, PA, 16802

[3] Science and Technology Corporation, Hampton, VA, 23666

[4]Lawrence Livermore National Laboratory, Livermore, CA, 94550

[5] University of Utah, Salt Lake City, UT, 84112

Keywords: high-energy diffraction microscopy (HEDM); residual stress; high-cycle fatigue (HCF); fatigue indicator parameter (FIP); crystal plasticity

Abstract

Far-field high-energy X-ray diffraction microscopy (ff-HEDM) and the crystal plasticity finite element method (CPFEM) are used to investigate the role of grain-scale (Type-II) residual stresses on the fatigue life of additively manufactured (AM) Inconel alloy 625 (IN-625). Grain-averaged orientations, centroids, and residual elastic strain tensors from ff-HEDM data are used to instantiate a crystal plasticity model to simulate the effect of residual stresses at the grain scale. Simulation results indicate that the presence of tensile residual strains increase stress localization and heterogeneity within grains, triggering an earlier onset of plasticity. A microscale fatigue indicator parameter (FIP) is computed to model the impact of these residual strains on the cycles to fatigue crack nucleation. The crack nucleation model, based on the computed FIPs, predicts a significant reduction in the number of cycles for fatigue crack nucleation for mid- and high-cycle fatigue due to the residual strain induced localization, while the residual strains have minimal impact on low-cycle fatigue life.

1. Introduction

Additive manufacturing (AM) has emerged in the last decade as one of the most investigated manufacturing methods in materials and processing research. Interest is due to the promise of increased manufacturing rate and cost savings for near-net shape production of parts with low production volume, complex geometric design requirements, or made from valuable materials. Broad potential structural applications exist for many AM alloy systems including aluminum, nickel, steel, and titanium. However, it is now well known that qualification and certification of AM structural components to-date has been largely precluded by high variability in mechanical behavior and fatigue cracking issues, due in part to build anomalies, surface roughness, and processing-induced defects [1–4]. Specific to this paper, nickel-based superalloy AM materials include potential fatigue critical applications such as combustion chambers, casings, turbines, discs and blades for high-pressure aircraft engines along with valves, ignitors, injectors, turbomachinery, and manifolds for liquid rocket engines [5]. However, improvements to AM processes and materials are first needed to improve repeatability and, in turn, improve fatigue performance and reliability. Processing improvements to increase fatigue performance and decrease variability, coupled with the development of robust computational modeling tools will aid in qualification and certification efforts.

As a contextual baseline, fatigue has been relatively well studied for conventionally manufactured materials with decades of observations both in the lab and in practice. This history has resulted in materials and processing enhancements to improve fatigue performance. Additionally, modeling and simulation tools have evolved in parallel to establish improved practices for safe design. However, even with conventional materials and manufacturing, fatigue remains the most common failure mechanism in structural metals in practice [6] where an estimated 90% of failures, especially in rotating metallic parts are attributed to fatigue [6,7].

In contrast to conventional materials, AM is relatively new and associated with increased mechanical property variability, e.g., fatigue life [8], that exceeds that of conventionally manufactured materials. Laser powder bed fusion (LPBF), for example, is a popular layer-by-layer

AM method [9,10] in which a new layer of powder is added and consolidated in repetition until the desired part geometry is complete. While LPBF provides many benefits including high-dimensional accuracy, material challenges exist which complicate the qualification and certification of LPBF-produced parts. Corresponding structural integrity issues for AM-produced parts have been investigated [3,11], including processing-induced defects, surface roughness, and residual stresses. Generally, increases in each of these characteristics reduces fatigue life and increases scatter in LPBF compared to wrought counterparts [12]. To date, processing-induced defects and surface roughness have largely been the focus of fatigue crack initiation mechanisms in AM applications [13]. Consequently, a brief review of effects-of-defects and roughness studies is provided before shifting focus toward the impact of residual stresses on fatigue cracking, the effects of which are yet to be quantified and are the focus of this study.

Surface roughness and porosity in LPBF parts currently receive significant attention due to fatigue cracking concerns. If present, porosity and surface roughness generally are more deleterious for fatigue performance compared to residual stresses [9]. While the impact of residual stresses on fatigue crack initiation remains relatively unknown, it can be expected that such stresses will naturally alter the heterogeneous interactions at the microscale, and in turn, the fatigue life [14]. For example, compressive residual stresses can enhance fatigue life, while tensile residual stresses are typically undesirable due to reducing fatigue life [15]. For LPBF, residual stresses originate from large thermal gradients associated with the high local heat input and subsequent rapid cooling rates of the LPBF process [10]. Generally speaking, residual stresses can be classified as one of three types [16]. Type-I refers to long-range (continuum scale) residual stresses that equilibrate over the scale of the part. Type-II residual stresses equilibrate over multiple grains (estimated 3 grains to 10 grains). Type-III residual stresses equilibrate within a single grain over a range estimated from the atomic scale to less than the grain size. The focus of this paper is the role of Type-II residual stresses on fatigue life.

To date, published studies on the impact of residual stress on AM material performance have focused on Type-I stresses, with focus on manufacturing part deformation resulting in distortion

or deviance from the desired shape [8,16–18]. In addition to distortion, Type-I residual stresses accelerate material degradation by negatively impacting fatigue life, corrosion, and fracture toughness performance [19,20]. Type II and III residual stresses contribute to the heterogeneous stress distribution at the same length scale where fatigue cracks initiate and propagate. Type-II and III residual stresses have seen less attention than Type-I stresses. However, these microscale residual stresses have been associated with macroscopic tension-compression asymmetry and work hardening [21]. Since fatigue damage most often initiates at the microscale, consideration of the Type-II and III distributions is important to accurately predict high-cycle fatigue performance [22,23].

In these past studies, however, experimental quantification of residual strains have either lacked the ability to spatially-correlate the measurements with location or microstructure (e.g., X-ray [24] or neutron diffraction [25,26]), or destructively altered the state of residual stress and lacked the ability to characterize the distribution in the full three-dimensional volume (3-D) (e.g., high-resolution electron backscattered diffraction [27]). However, recent development of the high-energy X-ray diffraction microscopy (HEDM) at beamline facilities enables measurement of the grain-averaged local stress/strain fields and crystallographic orientation in 3-D volumes [22,28,29]. Therefore, initial grain-scale residual strains (Types-II and III) can now be measured via HEDM and transformed into stresses via Hooke's Law to assess residual stresses and provide the required data for model instantiation [30].

The objective of this study, therefore, is to use HEDM to measure Type-II residual strains in an LPBF Inconel alloy 625 (IN-625) specimen and simulate the role of Type 2 residual stresses in the fatigue response of AM Inconel 625. To this end, the measured strains are used to initiate the crystal plasticity model stress state, using HEDM-generated experimental data (grain orientation, centroids, and residual strain tensors) using the approach of Kapoor and Sangid [22,28]. To further understand the impact of the residual strains, baseline models without the residual strains are simulated for comparison of fatigue life predictions. To the authors' knowledge, these simulations provide a first example of combining these HEDM measurements

with crystal plasticity to study the effect of residual stresses on fatigue crack initiation in AM materials.

Ultimately, results from these crystal plasticity simulations are sought to be used for fatigue life estimates. However, the underlying microstructure heterogeneity (crystal orientation, grain boundaries, etc.) at the scale of Type-II and III residual stresses leads to a similitude breakdown, which is required for application of linear elastic fatigue and fracture principles [31]. To accommodate this breakdown, the impact of heterogeneous microscale plastic flow on fatigue crack initiation [10,15] is modeled using fatigue indicator parameters (FIPs). FIPs have been proposed to account for these microstructure sensitive variables in relation to the likelihood of creating a MSFC [33–38]. Recently, a crystallographic FIP derived from the work of Fatemi-Socie [39] has been shown to correlate with crack growth (*da/dN*) rates [34,37]. This crystallographic version of the Fatemi-Socie FIP is utilized in this work to assess the variability for high cycle fatigue (HCF) considerations due to residual stresses. The Fatemi-Socie FIP is known to correlate well with the early crystallographic stages of crack growth connected to planar slip in metals [34].

The paper is organized by the following sections. The material tested, and experimental and computational methods utilized will be described in Section 2. The results from both the experimental testing and crystal plasticity simulations, quantifying the initial residual strains and simulating the impact of those residual strains on the micromechanical response at the grain scale will be presented in Section 3. The pertinent implications of the observations presented in Section 3 will be discussed in Section 4, leading to the summary, conclusions, and future work being discussed in Section 5. In summary, significant Type-II residual strains were observed. These strains are predicted to increase both the magnitude and heterogeneity of the local stress state within grains during macroscopically elastic loading, promoting higher FIP values and reduced HCF life.

2. Materials and Methods

2.1 Material

The IN-625 specimen used in this study was produced by LPBF at the National Institute of Standards and Technology (NIST) in an EOS INT M290 machine[ϕ]. The IN-625 powder was supplied by EOS and the chemical composition is provided by Lass, *et al.* [40]. Printing parameters included a laser power of 285 W and laser velocity of 960 mm/s, per the EOS manufacturer recommendation. The build layers were 40 μm tall and the hatch distance was 110 μm, producing a block of dimension 25.4 mm X 25.4 mm x 32 mm. Prior to removing the block from the build plate with wire electro-discharge machining, the material was stress relief heat treated at 800°C for 1 hr. Once removed, the block was then hot isostatic pressed (HIP) to reduce internal porosity at 152 MPa and 1175°C for 4 hr in an Ar atmosphere following ASTM F3056. The HIP process also promoted recrystallization in the material. A previous study found that this material and processing had equiaxed grains of approximately 40 μm in diameter with relatively low misorientation across the grains [41], suggesting a recrystallized microstructure with significantly reduced dislocation content in comparison to the as-built state. A small tensile specimen with 1 mm x 1 mm square cross section was extracted from the block with the tensile axis oriented parallel to the build direction. We note that extraction of the specimen from the block is expected to relieve any remaining Type-I residual stresses present. A picture of the IN-625 HEDM test specimen is shown in Figure 2A. A thorough description of the specimen geometry and testing setup specific to the RAMS2 load frame is provided in Ref. [42].

[ϕ] Specific vendor and manufacturer names are explicitly mentioned only to accurately describe the test hardware used. The use of vendor and manufacturer names does not imply an endorsement by the U.S. Government, nor does it imply that the specified equipment is the best available.

2.2 HEDM Testing

The extracted tensile specimen was mounted in the RAMS2 load frame [43] in ID-1A3 beamline at the Cornell High Energy Synchrotron Source (CHESS). Far-field HEDM (ff-HEDM) measurements were then performed using the experimental geometry shown in Figure 1. The ff-HEDM technique is capable of non-destructively reconstructing grain-averaged center of mass, lattice orientation, and elastic strain state of individual grains within polycrystals (all of which are used for crystal plasticity finite element method (CPFEM) model instantiation). A more complete description of HEDM (or 3DXRD) methods can be found in [44], but a brief description of ff-HEDM is provided.

Far-field HEDM is a transmission, rotating crystal X-ray technique. Diffraction patterns are measured on area detectors sitting approximately 1 m behind the specimen as a specimen is rotating around a single axis and fully illuminated (similarly to X-ray computed tomography). Critically, the microstructure must be such that individual diffraction peaks are measured on the area detector(s) as opposed to continuous diffraction rings (see Figure 1). The microstructure reconstruction from the diffraction pattern works by using a forward projection technique to simulate where diffraction peaks will occur on the area detector(s) *from all possible crystallographic orientations*. If a certain number of peaks from a tested orientation is found on the detector (usually more than 90%), the orientation is determined to be present and the peaks are associated with that orientation (i.e., a grain). Once the diffraction peaks are associated with a grain, a secondary optimization is performed to determine the position, orientation, and elastic strain state of the grain consistent with the peak positions measured as the sample was rotating. Usually over 50 diffraction peaks are used in this optimization process.

For the ff-HEDM measurements performed here, the specimen was illuminated using a 61.332 keV X-ray beam that was 2 mm wide x 1 mm tall creating a 1 mm^3 diffraction volume. The processing route described in the preceding subsection created a microstructure amenable for far-field high-energy X-ray diffraction microscopy (ff-HEDM) as individual diffraction peaks could be resolved on area detectors. As seen in Figure 1, diffraction data was collected on two Dexela

2923 area detectors that were 877 mm behind the specimen. Each detector had 3072 x 3888 pixels (horizontal x vertical), 74.8 μm pixel size, and were arranged with a vertical gap between the detectors as described in Ref. [42]. Prior to the experiment, far-field detector parameters (sample-to-detector distance, detector tilts, and detector distortions) were calibrated using a CeO_2 powder standard from NIST. Diffraction patterns were collected every 0.25° as the specimen was continuously rotated across a 360° range about the vertical axis. The specimen was incrementally loaded at an approximate strain rate of 1 x 10^{-6} over 38 steps to collect ff-HEDM data while the specimen was held under load. Inconel alloys do not exhibit significant strain rate sensitivity for quasistatic loading [45]. An optical camera collected images of the sample surface that were then processed using a custom digital image correlation (DIC) script to calculate macroscopic strains. Load cell output was used to calculate macroscopic stress.

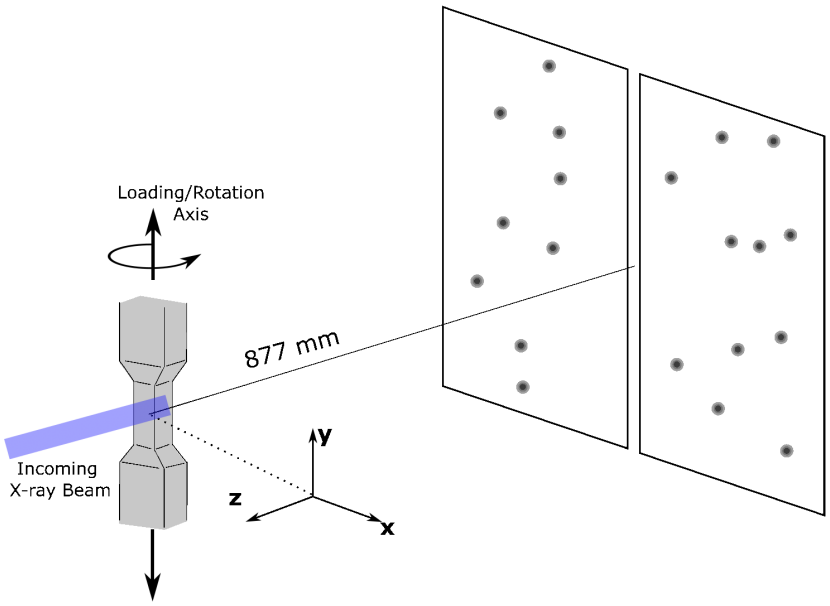

Figure 1. Schematic of the far-field high-energy X-ray diffraction microscopy experimental geometry for grain-scale residual elastic strain measurements.

The ff-HEDM data was reconstructed using the HEXRD software package [46]. A total of 298 grains were reconstructed in the diffraction volume in the unloaded state. The measured equivalent elastic strains $\epsilon_{HEDM-eq}$ (evaluated from the full elastic strain tensor) are plotted by their centroid positions in Figure 2B. These measurements originated within the 1 mm x 1mm

gauge section indicated by the boxed region on the test specimen image from Figure 2A. Some grains with high residual strains are clustered near the center of the volume. Typically, higher residual strains are expected near the edge of the build due to higher cooling rates [47]. However, in this case, near surface residual strains may have been relieved due to specimen fabrication with EDM. Grain-averaged stress tensors were computed from the measured elastic strain tensor $\boldsymbol{\epsilon}_{HEDM}$ using single crystal elastic moduli and anisotropic elasticity. Grain-averaged (Type-II) residual strain and stress tensors were evaluated in the unloaded state and used for subsequent model initialization. The lattice orientation error was approximately 0.01° and per component strain tensor error in this configuration was previously found to be approximately 10^{-4} [48]. A completeness threshold (number of diffraction peaks found in the data divided by the number of predicted peaks) of 0.95 and χ^2 threshold (self-consistency) of 0.02 were used to determine which reconstructed elastic strain tensors would be used for model instantiation. Residual stresses (σ_{Res}) were computed using the anisotropic form of Hooke's Law shown in Eq. 1.The following single crystal moduli were used to construct the stiffness tensor, $\mathbb{C}$: C_{11} = 243.3 GPa, C_{12} = 156.7 GPa, and C_{44} = 117.8 GPa. These values were obtained from computed values for IN-625 room temperature in-situ loading experiments using time-of-flight neutron diffraction referenced in Ref. [49].

$$\sigma_{Res} = \mathbb{C} \cdot \epsilon_{HEDM} \qquad \text{Eq. 1}$$

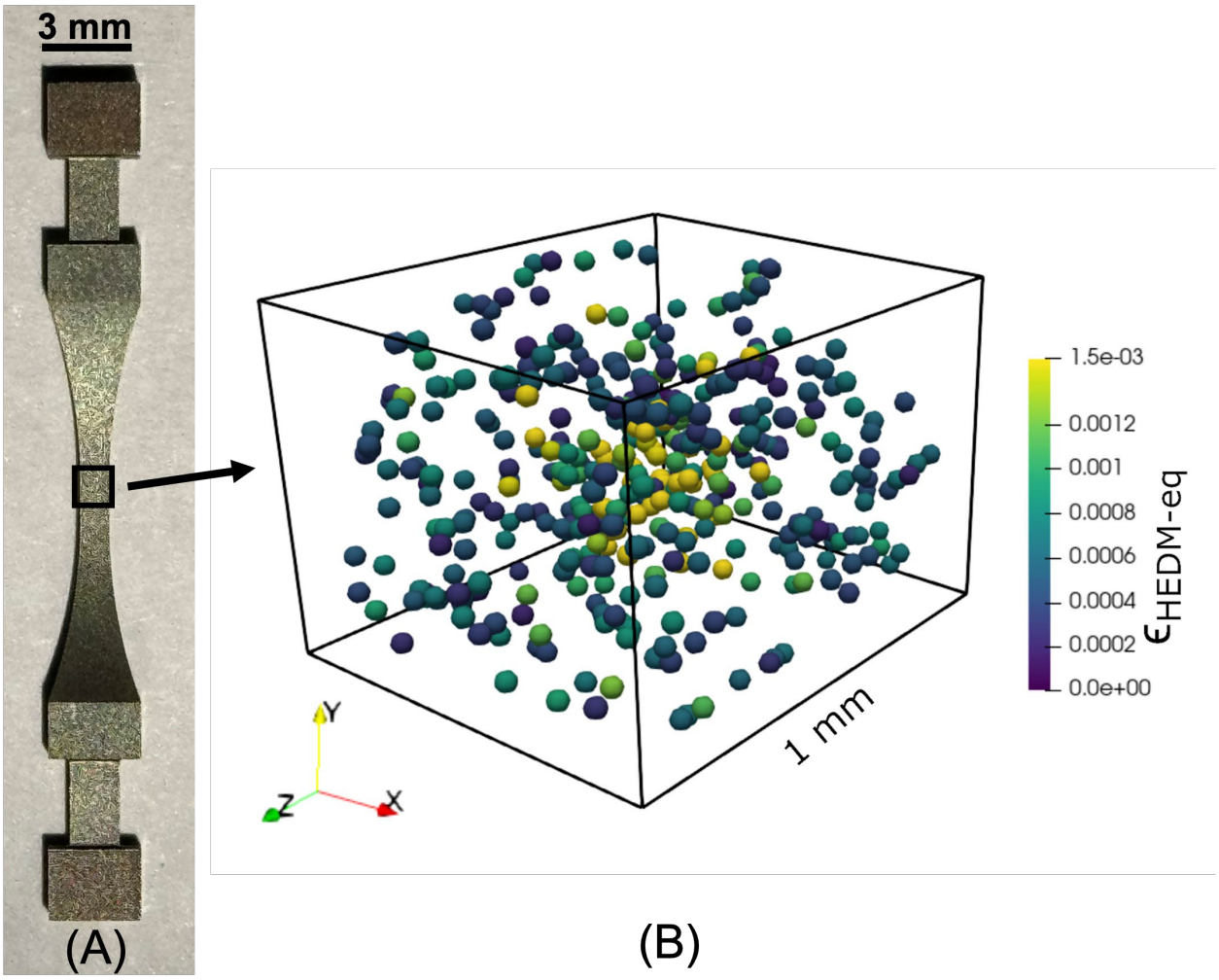

Figure 2. A) Photo of IN-625 HEDM test specimen. B) Residual equivalent strains ($\epsilon_{HEDM-eq}$) in the IN-625 specimens measured by ff-HEDM placed by their centroid positions collected from the 1 mm x 1 mm gauge section denoted by the boxed region in (A).

2.3 Crystal Plasticity Finite Element Modeling

The grain-averaged centroid data for all 298 grains present within the illuminated region of the gauge section during ff-HEDM are used to create a three-dimensional (3D) AM IN-625 volume using a Voronoi tessellation algorithm in NEPER [50]. Each grain in the tessellation is instantiated using the same grain orientations measured with ff-HEDM, so that the generated finite element model has an identical texture to that of the measured material volume. Gmsh [51] was then used to produce a finite element mesh (comprised of quadratic tetrahedral elements) for the tessellated

microstructure. The final mesh, shown in Figure 3, consisted of 1,766,590 nodes and 1,293,002 quadratic tetrahedral elements. Alongside the image of the mesh in Figure 3 is an image of the grain structure with inverse pole figure colors defined relative to the tensile axis (also the build direction). It must be noted that although the ff-HEDM technique effectively captures the centroids and crystal orientations of the grains, which is leveraged by the Voronoi tessellation algorithm, the grain boundaries are not precisely reconstructed. However, Kapoor and Sangid [28] demonstrated that a tessellated microstructure produces similar stress states as modeling the exact grain boundaries, indicating that any associated errors do not have a significant impact on the overall response.

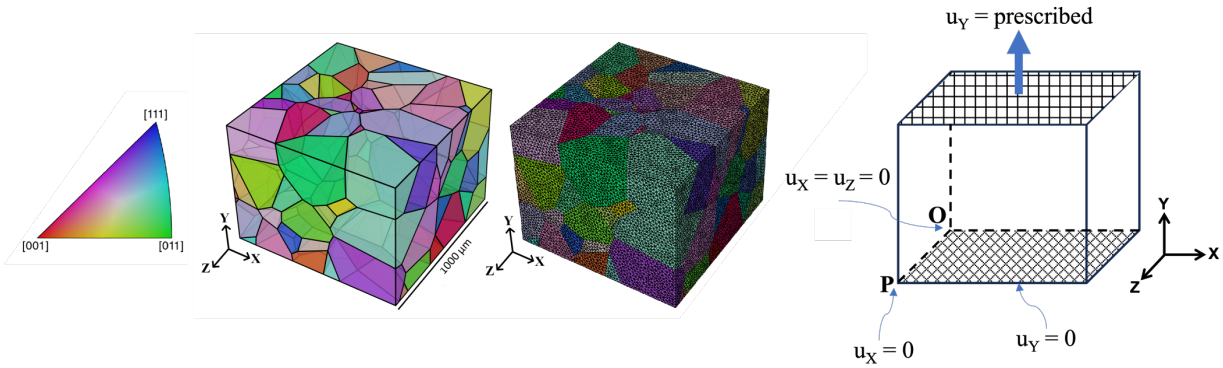

Figure 3. Tessellated microstructure (left) and mesh (center) colored based on IPF for the tensile / build axis with annotated boundary conditions (right).

The boundary conditions for the CPFEM were chosen to replicate the experimental conditions and are illustrated in the sketch in Figure 3. In the ff-HEDM experiment, the side faces of the gauge section of the specimen were free surfaces. The boundary conditions reflect traction-free surfaces on the side faces. The top surface (+Y) had a predefined displacement at a constant, linear rate corresponding to a strain rate of 1 x 10^{-6} simulating the tensile loading of the specimen in the Y-direction. The bottom surface of the model was restricted to move in the Y-direction. Two corners on the bottom face were fixed to constrain against rigid body motion, mirroring the approach described by Stopka, *et al.* [35]. Specifically, the node at the origin (point O) was constrained in X- and Z-directions, and one node was fixed in the X-direction at point P.

The NASA open-source, parallel finite element package ScIFEN was utilized for crystal plasticity simulation [52]. ScIFEN was used to simulate the effect of initial residual strains to solve for the heterogeneous state of stress within the polycrystalline IN-625 specimen, using anisotropic elasticity and rate-dependent CP kinetics. The single crystal elastic moduli C_{11}, C_{12}, and C_{44} provided in Section 2.2 were utilized to model the elastic response (values obtained from [49]).

The simulated plastic deformation proceeds via crystallographic slip along the 12 FCC slip systems – {111}<110> family. The slip system shearing rate, $\dot{\gamma}^{\alpha}$, for the α^{th} slip system (12 total) is derived from the plastic velocity gradient in the intermediate configuration as,

$$L^P = \dot{F}^P (F^P)^{-1} = \sum_{\alpha} \dot{\gamma}^{\alpha} (s^{\alpha} \otimes n^{\alpha}) \,, \quad \text{Eq. 2}$$

where L^p is the plastic velocity gradient, $\dot{F}^P$ is the plastic deformation rate, s^{α} is the slip direction and n^{α} is the slip plane normal for the α^{th} slip system. The flow rule describing incremental slip on the 12 FCC slip systems is given by,

$$\dot{\gamma}^{\alpha} = \dot{\gamma}_o \frac{\tau^{\alpha}}{g^{\alpha}} \left| \frac{\tau^{\alpha}}{g^{\alpha}} \right|^{\frac{1}{m}-1}, \quad \text{Eq. 3}$$

where $\dot{\gamma}_o$ is the reference slip system shearing rate, τ^{α} is the slip system resolved shear stress, g^{α} is the slip system critical resolved shear stress, and m is the material rate sensitivity exponent. The recrystallization that occurred during HIP'ing significantly reduced the dislocation content present within the grains (as evidenced by the minimal intragranular misorientation [41]) reducing the need for an Armstrong-Frederick type backstress term in the flow rule. The Type-II residual stresses instantiated within the grains will effectively shift the yield surface of each grain, producing an effective back stress.

The slip system resistance $\dot{g}^{\alpha}$ evolves according to Eq. 4 based on Voce-Kocks relations [53]

$$\dot{g}^{\alpha} = G_o \left(\frac{{g_s}^{\alpha} - g^{\alpha}}{{g_s}^{\alpha} - {g_o}^{\alpha}} \right) \sum_{\alpha} |\dot{\gamma}^{\alpha}| \,, \quad \text{Eq. 4}$$

where G_o is the initial hardening rate, ${g_o}^{\alpha}$ is the athermal portion of the initial (reference) critical resolved shear stress, and ${g_s}^{\alpha}$ is the saturation critical resolved shear stress.

Grain-averaged (Type-II) residual strains from ff-HEDM were initialized in CP model through modification of the finite strain multiplicative decomposition of the deformation gradient into elastic and plastic parts, following Lee [54],

$$F = F^E F^P, \qquad \text{Eq. 5}$$

where F is the total deformation gradient tensor, which is decomposed into an elastic component F^E and a plastic component F^P. Eq. 5 was modified with the insertion of a third deformation gradient tensor F^R referred to as the residual deformation gradient tensor,

$$F = F^E F^R F^P. \qquad \text{Eq. 6}$$

The approach mirrors that described in Refs. [22,28]. Consistent with the ff-HEDM experiment, the specimen is initially undeformed in the presence of the residual stresses, hence $F = I$ at the start of the simulation, where I is the identity tensor. Similarly, $F^P = I$ at the start of the simulation. Therefore, to maintain the relationship in Eq. 6, F^E must equal $(F^R)^{-1}$ at the start of the simulation. The initial elastic deformation gradient is determined through the following relationship,

$$F^E = I + \epsilon_{HEDM} \qquad \text{Eq. 7}$$

where, again, ϵ_{HEDM} is the grain-average elastic strain tensor measured via ff-HEDM. At the initial load step, the measured stress from the load cell was -2.56 MPa. Given the relatively low stress, the strains due to the applied load at the start of the test are negligible. Throughout the simulation, F^E evolves with applied deformation. However, F^R is held constant based on the value determined at the initial load step,

$$F^R = {F^E}^{-1}\Big|_{t=0} = (I + \epsilon_{HEDM})^{-1}. \qquad \text{Eq. 8}$$

As noted by Refs. [22,28], F^R is an eigen deformation gradient tensor and does not produce a stress field but only acts to maintain consistency in Eq. 5 by ensuring $F = F^P = I$ at the start of the simulation.

At the microscale, several parameters are examined to assess the magnitude and impact of the residual stresses. The first parameter is the von Mises stress, σ_{VM}, shown in Eq. 9, which is obtained from the computed stress tensor, σ.

$$\sigma_{VM} = \sqrt{\frac{3}{2}\sigma : \sigma} \qquad \text{Eq. 9}$$

The second parameter is the mean stress, σ_M, which is the average of the normal stress components, σ_{xx}, σ_{yy}, σ_{zz},

$$\sigma_M = \frac{1}{3}\left(\sigma_{xx} + \sigma_{yy} + \sigma_{zz}\right). \qquad \text{Eq. 10}$$

The third parameter is the Fatemi-Socie FIP based on the combined effect of normal and shear stresses acting on a slip plane [39]. Eq. 11 defines the microscale version of the Fatemi-Socie FIP parameter used here, where *k* is a proportionality constant, σ_n^p is the normal stress acting on a given slip plane, *p*, and σ_y is the macroscopic yield stress. In the case of FCC materials, the Fatemi-Socie FIP parameter is computed as the maximum value over all four {111} slip planes, *p*, for the integral shown below with respect to time, *t*.

$$FIP = \max_p \int_0^t |\dot{\gamma}^\alpha| \left(1 + k\frac{\sigma_n^p}{\sigma_y}\right) dt \qquad \text{Eq. 11}$$

3. Results

3.1 ff-HEDM residual strain measurements and macroscopic tensile response

The maximum, minimum, average, and standard deviation of the residual stress components determined from the residual $\boldsymbol{\epsilon}_{HEDM}$ values are provided in Table 1. The maximum and minimum residual stresses are on the order of the magnitude of the YS (365 MPa). As can be seen, the average values are close to zero, indicating that the Type-I residual stresses are arguably negligible, as expected from a small volume extracted from a block. However, at the grain level, significant Type-II residual stresses exist. The standard deviation for each stress component indicates the wide scatter in stress values from grain to grain.

Table 1. Max, min, average, and standard deviation for the grain-averaged stress tensor components computed from ff-HEDM.

MPa units	σ_{xx}	σ_{yy}	σ_{zz}	σ_{xy}	σ_{xz}	σ_{yz}
max	319.2	354.4	267.9	147.1	168.9	163.8
min	-317.4	-314.3	-457.1	-142.6	-315.0	-150.4
avg	13.5	-2.8	5.9	-0.4	0.2	2.8
std dev	82.2	108.5	88.5	39.2	49.1	41.4

A histogram of the grain-averaged residual von Mises stresses for all 298 grains is shown in Figure 4. The average across all 298 grains is 153 MPa, which is approximately 42% of the observed YS, with a standard deviation of 80 MPa. The maximum grain-average von Mises stress was 592 MPa (162% of YS) and the minimum was 26 MPa (7% of YS).

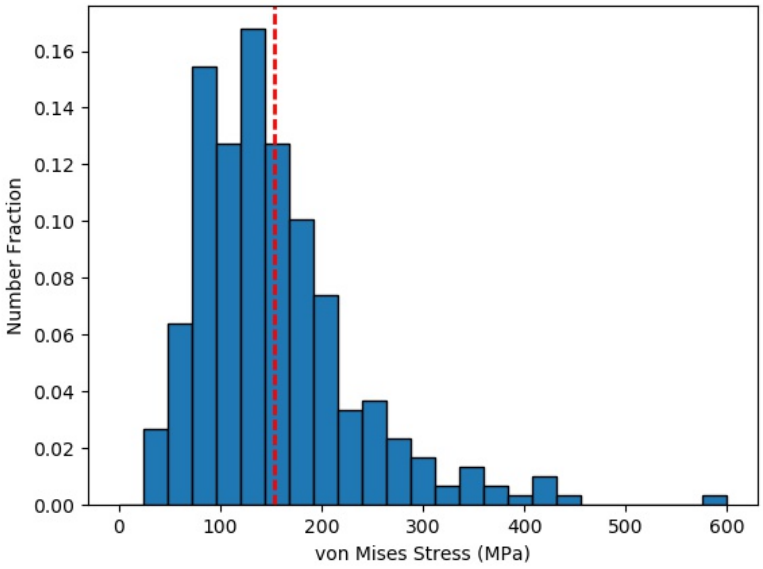

Figure 4. Histogram of grain-averaged residual von Mises stress computed from ff-HEDM measurements. Red dashed line indicates the average von Mises stress of 153 MPa.

A histogram of the grain-averaged residual mean stress from ff-HEDM are plotted in Figure 5. Of the 298 grains, 157 grains (53%) had tensile mean stress, while 141 (47%) had compressive mean stresses. The minimum and maximum grain-average mean stresses were -299 MPa and 298 MPa, respectively. The average mean stress across all grains was 5 MPa with a standard deviation of 77 MPa.

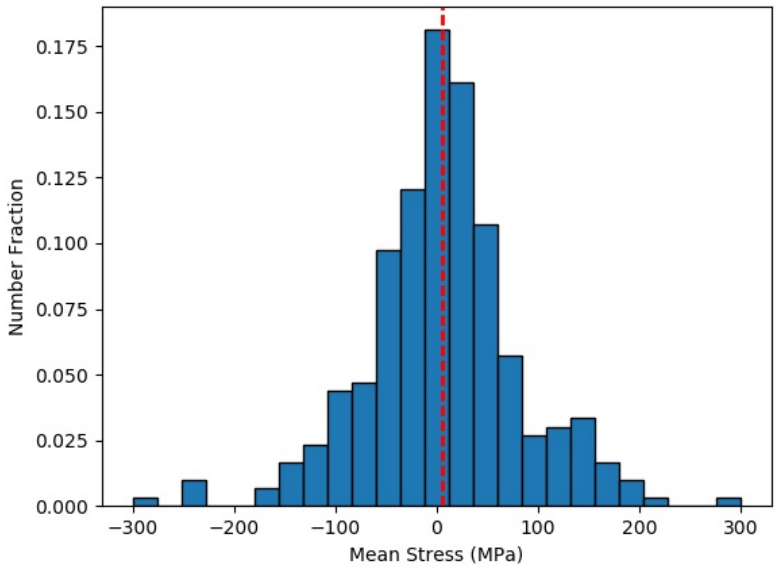

Figure 5. Histogram of grain-average mean stresses computed from ff-HEDM data. Red dashed line indicates the average mean stress of 5 MPa.

The macroscopic tensile stress-strain curve from the IN-625 specimen is shown in Figure 6. Each of the 38 circles indicate a point where DIC strain measurement was performed during straining. The IN-625 specimen was loaded to a maximum engineering strain of 3.2% and maximum engineering stress of 463 MPa. The 0.02% offset yield strength (YS) was measured to be 365 MPa, comparable to the YS for heat-treated LPBF IN-625 reported in [55].

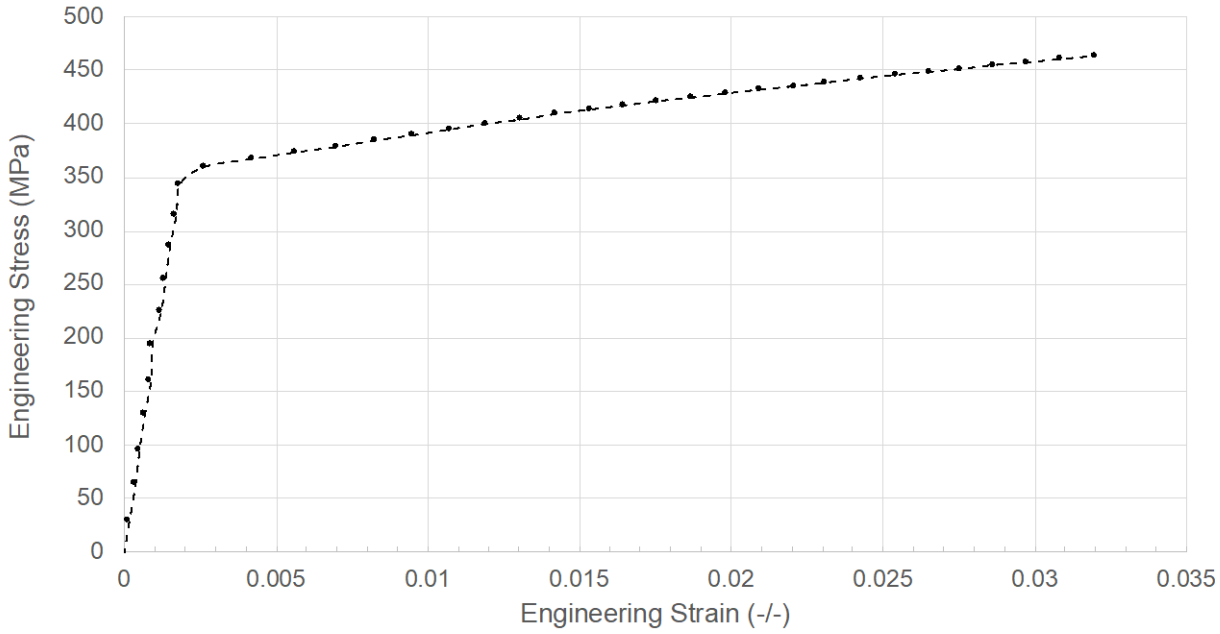

Figure 6. IN-625 stress-strain curve loaded in the build direction measured via DIC after ff-HEDM residual strain measurements.

3.2 CPFEM calibration and macroscopic results

The CPFEM parameters were calibrated to match the macroscopic response observed in Figure 6 from the ff-HEDM experiment. Calibration was achieved by iterative adjustment of the hardening parameters for simulations with the residual strains included. Calibrated values for the hardening parameters referenced in Eqs. 3 and 4 are provided in Table 2. These same values were utilized for simulations that did not include residual strains to facilitate a comparison of the effect of the residual strains on the macro- and microscopic response.

Table 2. Calibrated IN-625 CP hardening model parameters.

$g_o{}^{\alpha}$	152 MPa
$g_s{}^{\alpha}$	820 MPa
G_o	400 MPa
$\dot{\gamma}_o$	0.001 s^{-1}
m	0.006

The macroscopic engineering stress-strain curves from the calibrated CPFEM simulation results with and without the residual strains are plotted in comparison to the ff-HEDM results in

Figure 7. In both cases, the CPFEM results replicate the measured ff-HEDM experimental response well, indicating the parameters are well-tuned to match the experiment. Macroscopically, the two stress-strain curves differ by less than 4 MPa in the linear elastic region, but a divergence of ~3% between the two CPFEM simulations is observed during initial yielding in the elastoplastic transition. The inclusion of residual strains lowers the proportionality limit, indicating an earlier onset of bulk plasticity. The reduction is attributed to an overall majority of tensile residual stresses lowering the applied stress needed to initiate plastic deformation. The predicted divergence in the elastoplastic transition due to the inclusion of residual strains is consistent with observations in [29], except in their case the residual stresses were compressive in nature resulting a delayed elastoplastic transition. While the difference between the two simulations is relatively small, it suggests that some grains will yield significantly sooner due to higher tensile residual strains. For fatigue applications, extreme value statistics and the tails play an important role in fatigue life and crack nucleation. Therefore, the observed difference in the elastoplastic transition is likely foreshadowing of larger grain-scale differences in plasticity that may significantly impact fatigue performance.

There are clear fluctuations in the experimental curve in the elastoplastic transition shown in Figure 7 due to the nature of the DIC measurement, which makes calibration model parameters difficult in this region. Overall, the simulated stress-strain curves match well. While the simulated case without residual strains gives the appearance of a better match to the experimental data within the elastoplastic region, the uncertainty of the experimental measurement in this region is in question. Thus, it may be improper to conclude that the simulated response without residual strains provides a better match to the data given the uncertainty of the experimental measurements in the elastoplastic transition region. Both simulations yield slightly sooner than the measured response from the ff-HEDM experiment. However, the two curves reconverge at roughly the 0.02% offset YS. Therefore, the maximum difference in the macroscopic stress-strain response due to the inclusion of the residual strains is contained within the elastoplastic transition zone.

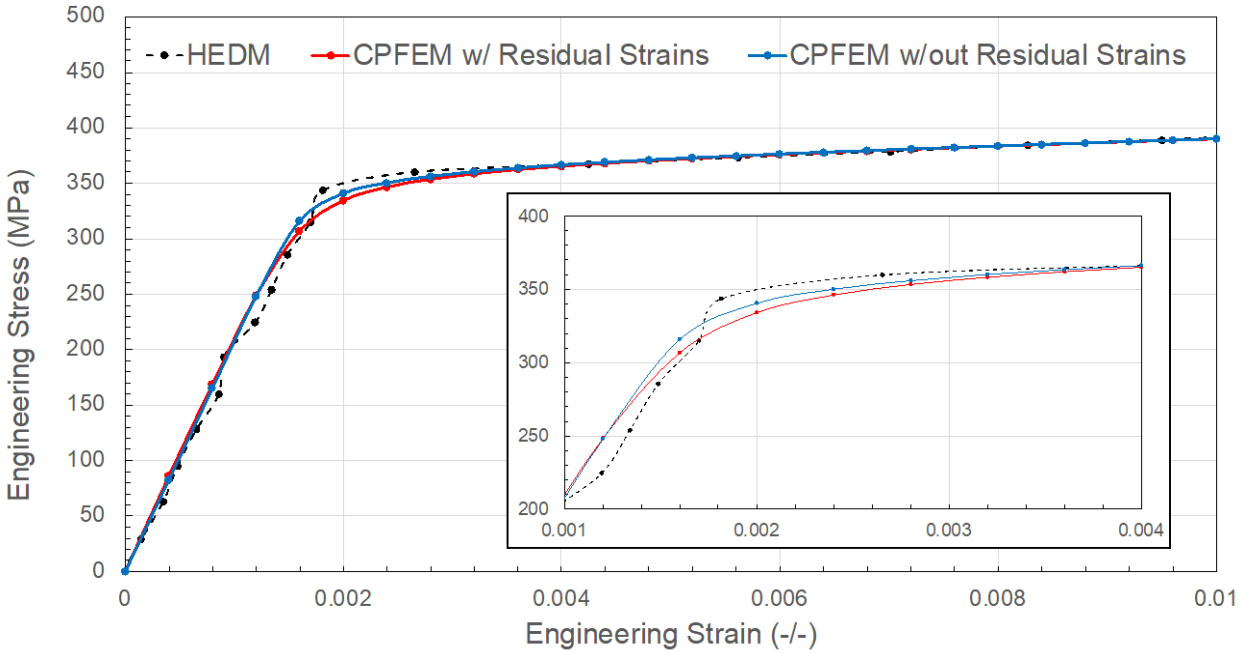

Figure 7. CPFEM with (red) and without (blue) residual strains vs. ff-HEDM (black) macroscopic stress-strain response with a zoomed in view near the elastoplastic transition.

3.3 Grain-scale CPFEM results

The effect of the initial residual strains was examined after an applied infinitesimal macroscopic strain (e_{macro}) of 1 x 10^{-6} with and without residual strains to compare stresses after equilibration in Figure 8. When the initial residual strains are neglected, the stresses within the microstructure are negligible (less than 0.4 MPa), demonstrated by the dark blue color in the figure. In contrast, when initial residual strains are included, simulation results show several hot spots where stresses exceed ~40% of the YS. These initial hots spots after equilibration from the initially prescribed grain-averaged strains from HEDM tend to accumulate at the grain boundaries and broadly across the interior of a handful of grains.

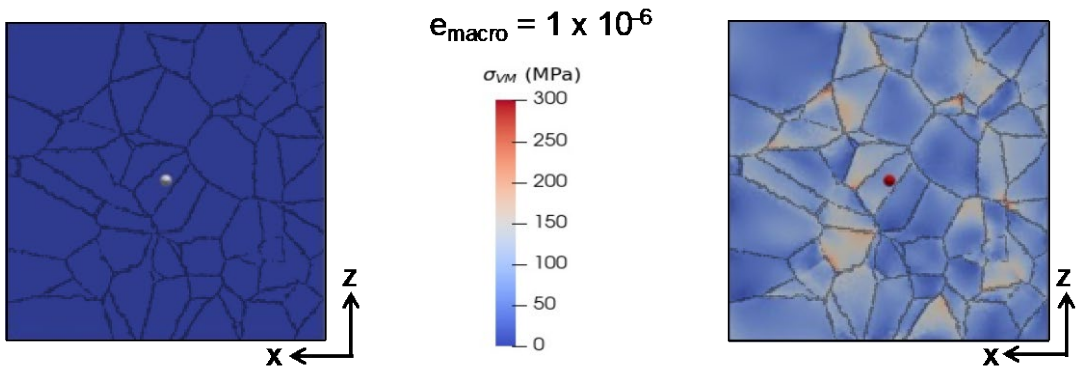

Figure 8. CPEM simulated von Mises stress plots (left) without residual strains and (right) after equilibration under a small strain of 1 x 10^{-6}.

To quantify the effect of residual strains as the macroscopic loading increases, the microscale von Mises stress distribution was extracted at five simulated macroscopic strain values of 0.4, 0.8, 1.6, 2.0, and 4.4 x 10^{-3}, which are annotated on the macroscopic stress strains curves in Figure 9. The von Mises stress plots are presented in Figure 10. The two-dimensional (2-D) plots were generated at the center of the gauge volume perpendicular to the tensile (Y) axis, i.e., on the X-Z plane. The center of the gauge section was selected to avoid any local effects associated with boundary conditions.

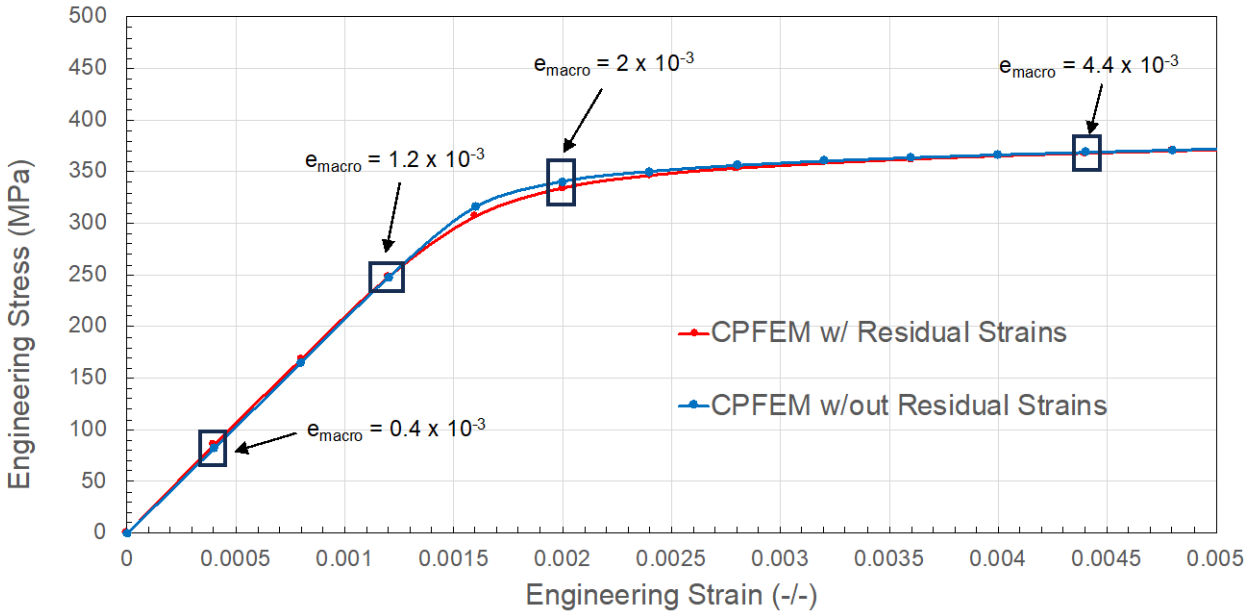

Figure 9. Load steps from the macroscopic stress-strain curve interrogated at the microscale in subsequent figures shown by the boxes with corresponding macroscopic strains noted.

The von Mises stress plots, Figure 10, reveal two important microscale impacts due to the incorporation of residual strains. First, the predicted magnitude of the von Mises stresses are higher when residual strains are included when macroscopic strain values are below the yield point, i.e., below approximately 1.6 x 10^{-3}, despite insignificant differences in the macroscopic stress-strain response, Figure 9. The predicted stress hot spots emerge at lower strains when the residual strains are included, which will accelerate damage development and failure. Higher stresses are generally found near grain boundaries with some spread to the interior of a handful of grains within the 2-D cross-section shown. In some instances, different grains or even intragranular regions develop higher stresses due to the inclusion of residual strains compared to when residual strains are neglected. However, changes in the location of the stress hot spots only occurs for a small percentage of the grains shown when comparing the two simulations. The inclusion of residual strains has a larger effect on the magnitude of the hot spot more so than the location within the area examined. At higher macroscopic strains (e_{macro} > 1.6 x 10^{-3}) after the onset of bulk plasticity, both von Mises stress distributions evolve to become nearly identical.

Second, modeling the residual strains predicts increased stress heterogeneity, similar to observations reported in [56]. Similarly, not only are the hot spots of higher magnitude, but the cooler stress zones are lower magnitude, such that the stress gradients are increased throughout the microstructure. Strong heterogeneity in the von Mises stress also indicates more unfavorable stress imbalances between grains, particularly prior to bulk plastic deformation. The observed stronger heterogeneity is unfavorable for fatigue life as it may accelerate failure [56]. The pairing of crystallographically hard and soft grains has been associated with grain boundary cracking in other studies [57,58] due to local strain incompatibility. Therefore, fatigue cracks may nucleate at grain boundaries with large differences in the von Mises stress amplified by initial residual strains.

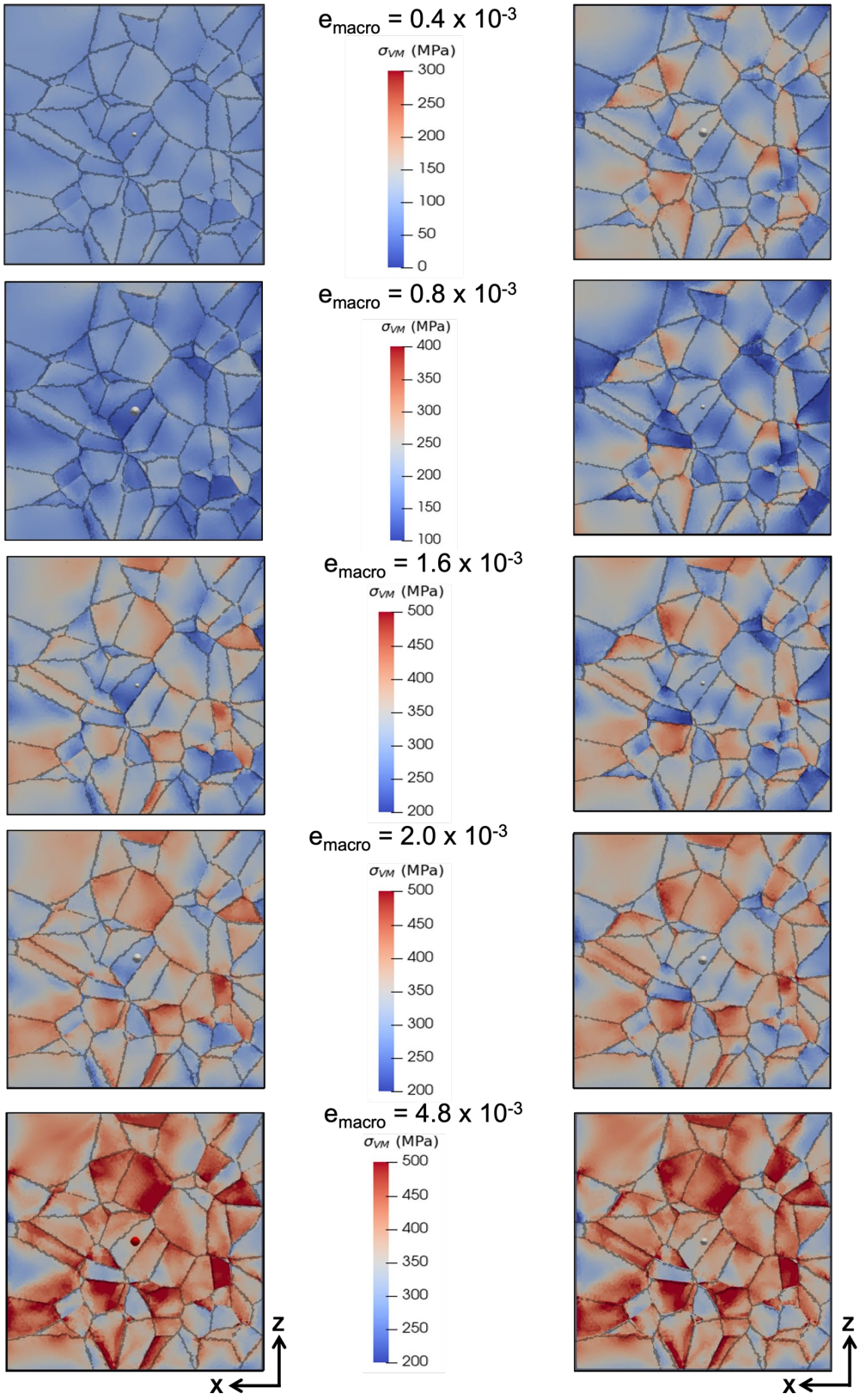
e_{macro} = 0.4 x 10^{-3}
σ_{VM} (MPa)
300
250
200
150
100
50
0
e_{macro} = 0.8 x 10^{-3}
σ_{VM} (MPa)
400
350
300
250
200
150
100
e_{macro} = 1.6 x 10^{-3}
σ_{VM} (MPa)
500
450
400
350
300
250
200
e_{macro} = 2.0 x 10^{-3}
σ_{VM} (MPa)
500
450
400
350
300
250
200
e_{macro} = 4.8 x 10^{-3}
σ_{VM} (MPa)
500
450
400
350
300
250
200
Z
X
Z
X

Figure 10. Simulated von Mises stress plots at increasing macroscopic strain levels with (right column) and without residual strains (left column). Note that the stress scale changes across the first three rows.

Similar to the von Mises plots in Figure 10, the FIP values for the same 2-D cross-sections are plotted for several macroscopic strain values denoted in Figure 11. Modeling residual strains resulted in significantly higher FIP values at lower strains. In the first row of Figure 9, FIP values are > 5 x 10^{-4}, when residual strains are incorporated, whereas FIP values are negligible (nominally zero) when residual strains are neglected. The significance of the difference in FIP values will be shown later in relation to predicted cycle count for nucleation. However, a FIP value of zero would imply infinite life and increasing FIP values correlating with shorter fatigue life. Not surprisingly, high FIP values correlate with grain boundaries and the locations with high von Mises stresses seen in Figure 10. Areas with higher FIP and von Mises stress values, particularly along grain boundaries, indicate potential fatigue crack nucleation sites. However, the FIP values are only associated with transgranular, not intergranular, crack initiation. Therefore, FIP values cannot be used to directly predict the likelihood for intergranular crack nucleation. With increasing strain, the FIP values increase in magnitude. Note the scale in the 2nd row of images in Figure 11 corresponds to a maximum FIP value of 5 x 10^{-3}. This is the same value where a fatigue crack was observed to initiate within ~ 100,000 cycles in [34]. However, the FIPs plotted in Figure 11 may not represent the extreme values for the entire 3-D microstructure. Further increases in the macroscopic strain led to increased FIP values with numerous other locations reaching 5 x 10^{-3} or greater when residual strains are modeled. As observed in the predicted von Mises stress results, the predicted FIPs with and without residual strains converge near yield. Ultimately, for the maximum macroscopic strain shown post-yield, the two cases are indistinguishable.

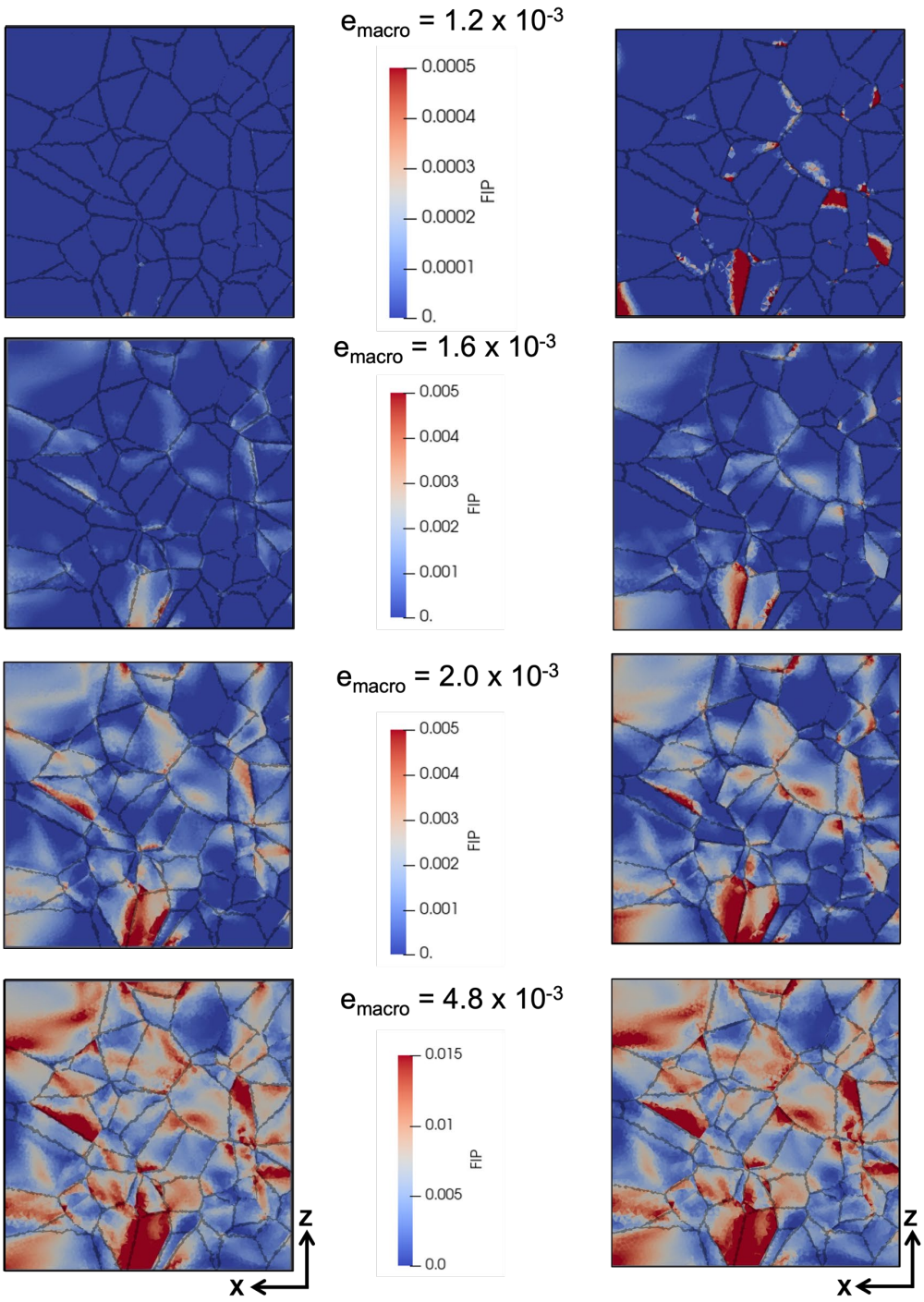

Figure 11. Simulated FIP plots at increasing macroscopic strain levels with (right column) and without (left column) residual strains.

3.4 Impact of residual strains on fatigue life

Fatigue crack nucleation is an extreme value problem, where grains with upper-tail FIP values generally limit fatigue life [59]. The FIP parameter has been previously demonstrated to have good agreement with experimental test data for prediction of fatigue life in HCF for an AM-produced aluminum alloy [60]. Castelluccio and McDowell [34] have established a relationship to experimentally calibrate the FIP parameter with the measured number of cycles to nucleate a fatigue crack (N_{nuc}) within a grain as shown in Eq. 12, where *A* is the irreversibility coefficient, d_{avg} is the average grain size, and FIP_{AVG} is the grain-averaged FIP value. Estimated N_{nuc} values computed from Eq. 11 have shown good agreement and reliability when compared to fatigue test data [60].

$$N_{nuc} = \frac{\mathrm{A}}{d_{avg}}(FIP_{AVG})^{-2} \qquad \text{Eq. 12}$$

Empirical cumulative distribution function (CDF) plots for the normalized grain-averaged fatigue life (number of cycles to nucleate a crack) for all 298 grains are provided in Figure 12. The empirical CDF plots were generated using the empirical CDF function in SciPy [61]. Multiple discrete CDFs are generated for several macroscopic strain levels from the simulations with and without the inclusion of Type-II residual strains. For some grains at low simulated strains, particularly when residual strains are neglected, the FIP_{AVG} values may be close to zero, generating unrealistically high fatigue life estimates. Hence, the maximum life plotted on the figure is 10^9 cycles. The normalized fatigue life was computed from Eq. 12. Lacking fatigue data for the LPBF IN-625 in this study, data is normalized by the leading term $\frac{\mathrm{A}}{d_{avg}}$ consistently across all modeled scenarios (in essence assuming the ratio equals to 1). Figure 12 indicates a significant reduction in the estimated number of cycles to crack nucleation due to the residual strains at lower macroscopic strains. In fact, the inclusion of residual strains reduces the normalized estimated cycles to nucleation by roughly three orders of magnitude or greater when $e_{macro} = 1.2 \times 10^{-3}$. At this macroscopic strain, only ~2% grains have predicted cycles to nucleation less than 10^9 when residual strains are not included, compared to ~30% when residual strains are included.

Additionally, the predicted cycles to nucleation for ~1% of the grains with were less than 10^6 cycles when residual strains were included for e_{macro} = 1.2 x 10^{-3}. As the macroscopic strain increases, the predicted cycles to nucleation tend toward convergence. After sufficient plastic strain (e_{macro} = 4.4 x 10^{-3}), the two CDFs are essentially equivalent. Therefore, the CDF plots further quantify the significant impact residual strains can have for HCF when cyclic strains are relatively low.

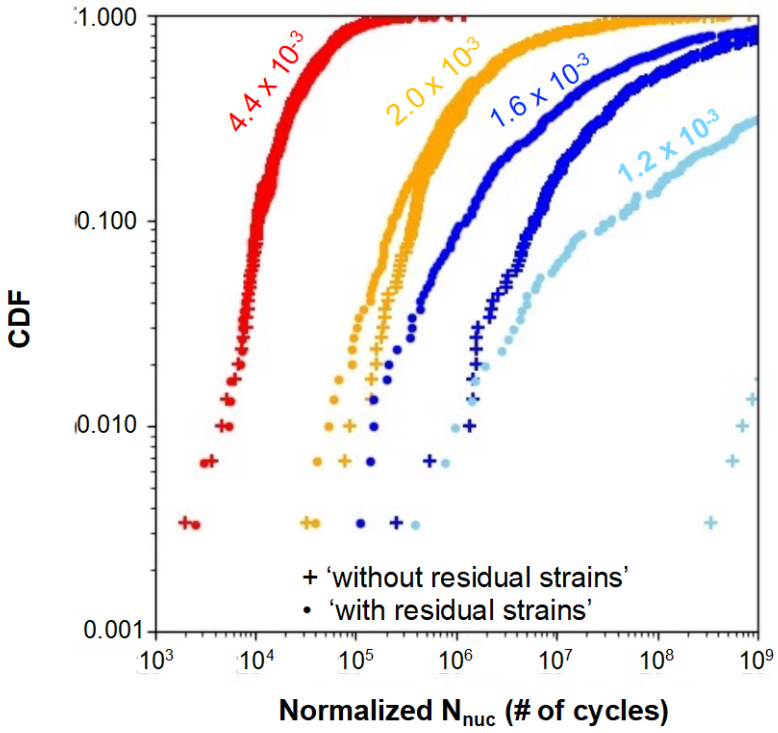

Figure 12. Empirical CDF plot of normalized N_{nuc} with and without residual strains included for multiple macroscopic strain levels from the simulation.

4. Discussion

The stress relief following standard commercial practice appears to have nominally relieved Type-I residual stresses (see average values in Table 1) but failed to relieve Type-II residual stresses at the grain-scale. The Type-II residual stresses measured in LPBF IN-625 specimen are significantly higher than expected, on the order of the yield strength of the material. Retained residual strains measured by ff-HEDM are likely lower than those in the initial build plate as the

sample has been excised with wire EDM, which likely would have relieved some residual stress. Therefore, the stress relieving heat treatment practice needs to be explored to ensure the heat treatment successfully mitigates processing-induced residual stresses, including Type-II residual stresses. Ff-HEDM provides a well-suited measurement technique through which to characterize the impacts of residual stresses. Failure to relieve Type-II residual stresses at the microscale may have significant impacts for qualification, certification, and safe service life, particularly for nickel-based superalloys given their usage in failure critical parts like turbine blades.

4.1 Importance of modeling Type-II residual strains in AM materials

In this study, the inclusion of initial Type-II residual strains shows a twofold effect, particularly prior to bulk plasticity. First, the residual strains added to the von Mises stress. Second, the residual strains increase the natural microscale heterogeneity in the von Mises stress from the CPFEM simulation when compared to the simulation without residual strains. The von Mises stress plots at lower strain values in Figure 10 show greater spread in the stresses at the grain scale. If the residual strains are significant, tension-compression asymmetry may be observed in the yield strength and strain hardening response [21]; however, compressive loading was not explored in this study. Often regions with strong heterogeneity occur along grain boundaries due to poor strain transfer. Therefore, the residual strains may increase the likelihood for grain boundary crack nucleation at these locations.

FIP values have been shown to correlate with crack growth driving force, with higher values leading to lower fatigue life. The inclusion of residual strains led to a significant increase in inter- and intra-granular heterogeneity at the elastoplastic transition which was captured by increased FIP values. As reported in [32,62], higher FIP values detrimentally impact fatigue life and, as such, the presence of residual strains and stresses, such as those found in the AM IN-625 specimen, will reduce fatigue life as described in more detail in this section.

Nominally, the hot regions in the ‘with residual stresses’ case emerge as hot regions in the ‘without residual stresses’ case. This observation indicates that the orientation of the grain and/or

the local neighborhood are the driving force for the location of the hot spot, not the initial residual strains. The residual strains simply amplify the overall magnitude of the FIP value. Therefore, residual strains will likely lower the number of cycles to fatigue crack initiation but may not alter the initiation location based on results in Figure 11.

After yield, the impact of the residual strains was unnoticeable as the two simulations are visually indistinguishable. The initial magnitude of the residual strains is small. Therefore, the simulation results suggest that, when the applied macroscopic strain exceeds the residual strain, residual strains are relieved and the associated effects are negligible. Therefore, residual strains are of greater concern for HCF rather than low cycle fatigue in agreement with Refs. [63,64].

4.2 Implications for application of LPBF and certification

A primary concern for Type-II residual stresses observed in this study will be for high cycle fatigue applications where microscale residual stresses will strongly influence fatigue life. This study indicates that, while stress relief heat treatment may nominally minimize Type-I residual stresses, significant Type-II residual stresses may be retained. Stress relief heat treatment at higher temperatures has been shown to relieve greater residual stress. Heat treatment at 750°C or higher has demonstrated a 50% or greater reduction in residual stresses [65]. However, above 800°C (the stress relief temperature in this study) the deleterious δ (Ni_3Nb) phase may precipitate along grain boundaries, melt pool boundaries, and interdendritic regions [65]. Considering this material concern, heat treating at a higher temperature may not be practical for IN-625.

Further study to correlate AM parameters with the associated microscale residual stress distributions are needed to guide AM process control to mitigate residual stresses [21]. Adaptation of processing parameters, like increasing power and decreasing scan velocity to reduce the solidification rate, can provide a reduction in the overall residual stress [66]. Additional post-processing steps that may reduce Type-II residual stresses and/or induce favorable compressive residual stresses may need to be explored to improve fatigue performance [10]. For fatigue-critical

applications, the minimization of Type-II, processing-induced residual stresses may be necessary for certification and to meet service life specifications.

5. Summary, Conclusions, and Future Work

Initial residual stresses were computed from ff-HEDM measured strains to reveal processing-induced residual stresses in a specimen from an IN-625 LPBF build. The following salient findings are provided from the ff-HEDM study:

- Ff-HEDM provided successful quantification of initial, Type-II residual strain tensors used to compute residual stresses, which is useful for assessing initial residual stresses and model instantiation.
- Standard post-processing failed to fully relieve residual stresses in an IN-625 LBPF specimen.
- Initial grain-averaged von Mises equivalent residual stresses estimated from ff-HEDM data ranged in magnitude from 26 MPa to 592 MPa (or 7% to 162% of the YS) with an average of 79 MPa (42% of YS). The grain-averaged mean stresses ranged from -299 MPa to 298 MPa with an average of 5 MPa.

Subsequent CPFEM simulation for the ff-HEDM microstructure with and without residual strains highlights the impact of the initial residual strains on mechanical performance. The CFPEM framework was successfully adapted to model initial ff-HEDM measured residual strains through the incorporation of the residual deformation gradient tensor, F^R. The following conclusions drawn from the CPFEM simulations results indicate that:

- Initial residual strains cause macroscopic yielding to initiate sooner, lowering the proportional limit compared to the simulation where residual strains were neglected.
- Residual strains influence the local stress hot spots and lead to increased heterogeneity within the microstructure compared to the simulation where residual strains were neglected.

- Initial residual strains significantly influence fatigue life estimates for high-cycle fatigue, lowering the estimated number of cycles to nucleation by several orders of magnitude.
- After sufficient plasticity has occurred, the effects of residual strains are negated and the two simulations with and without the inclusion of residual strains have similar local and global stress response and similar fatigue life estimates.

Future work should address strategies to minimize Type-II residual stresses through AM process modifications, particularly when high-cycle fatigue performance is required. Additionally, experimental fatigue testing of LPBF IN-625 specimens should be performed to calibrate fatigue life predictions provided in this study using Eq. 12. Calibration will enable modeling predictions in this paper to be validated using experimental fatigue test data. Finally, a baseline comparison of residual strains in IN-625 wrought versus AM microstructures should be completed. This comparison will provide insights into how the qualification of AM parts should be considered differently from conventional manufacturing approaches.

6. Acknowledgements

The HEDM work is based on research conducted at the Center for High-Energy X-ray Sciences (CHEXS), which is supported by the National Science Foundation (BIO, ENG and MPS Directorates) under award DMR-1829070. SRY was sponsored through the Research, Engineering, and Science Services (RSES) contract (80LARC23DA003) at NASA Langley Research Center.

7. References

[1] Seifi, M., Salem, A., Beuth, J., Harrysson, O., and Lewandowski, J. J., “Overview of Materials Qualification Needs for Metal Additive Manufacturing,” *Jom*, Vol. 68, No. 3, 2016, pp. 747–764. https://doi.org/10.1007/s11837-015-1810-0

[2] Seifi, M., Gorelik, M., Waller, J., Hrabe, N., Shamsaei, N., Daniewicz, S., and Lewandowski, J. J., “Progress Towards Metal Additive Manufacturing Standardization to Support

Qualification and Certification," *Jom*, Vol. 69, No. 3, 2017, pp. 439–455. https://doi.org/10.1007/s11837-017-2265-2

[3] Gorelik, M., "Additive Manufacturing in the Context of Structural Integrity," *Fatigue and Fracture Behavior of Additive Manufactured Parts*, Vol. 94, 2017, pp. 168–177. https://doi.org/10.1016/j.ijfatigue.2016.07.005

[4] Russell, R., Wells, D., Waller, J., Poorganji, B., Ott, E., Nakagawa, T., Sandoval, H., Shamsaei, N., and Seifi, M., "3 - Qualification and Certification of Metal Additive Manufactured Hardware for Aerospace applications**Disclaimer: The Views Presented in This Paper Are Those of the Authors and Should Not Be Construed as Representing Official Rules Interpretation or Policy of ASTM International, General Electric (GE), Lockheed Martin Corporation (LMCO), National Aeronautics and Space Agency (NASA), Japanese Space and Exploration Agency (JAXA), or the Federal Aviation Administration (FAA).," *Additive Manufacturing for the Aerospace Industry*, edited by F. Froes and R. Boyer, Elsevier, 2019, pp. 33–66. https://doi.org/10.1016/B978-0-12-814062-8.00003-0

[5] Gradl, P., Tinker, D. C., Park, A., Mireles, O. R., Garcia, M., Wilkerson, R., and Mckinney, C., "Robust Metal Additive Manufacturing Process Selection and Development for Aerospace Components," *Journal of Materials Engineering and Performance*, Vol. 31, No. 8, 2022, pp. 6013–6044. https://doi.org/10.1007/s11665-022-06850-0

[6] Courtney, T. H., "Mechanical Behavior of Materials," Waveland Press, Long Grove, IL, 2005.

[7] Meyers, M and Chawla, K, "Mechanical Behavior of Materials," Cambridge University Press, New York, 2009.

[8] Ye, C., Zhang, C., Zhao, J., and Dong, Y., "Effects of Post-Processing on the Surface Finish, Porosity, Residual Stresses, and Fatigue Performance of Additive Manufactured Metals: A Review," *Journal of Materials Engineering and Performance*, Vol. 30, No. 9, 2021, pp. 6407–6425. https://doi.org/10.1007/s11665-021-06021-7

[9] Gordon, J. V., Narra, S. P., Cunningham, R. W., Liu, H., Chen, H., Suter, R. M., Beuth, J. L., and Rollett, A. D., "Defect Structure Process Maps for Laser Powder Bed Fusion Additive

Manufacturing," *Additive Manufacturing*, Vol. 36, 2020, p. 101552. https://doi.org/10.1016/j.addma.2020.101552

[10] Denti, L., Bassoli, E., Gatto, A., Santecchia, E., and Mengucci, P., "Fatigue Life and Microstructure of Additive Manufactured Ti6Al4V after Different Finishing Processes," *Materials Science and Engineering: A*, Vol. 755, 2019, pp. 1–9. https://doi.org/10.1016/j.msea.2019.03.119

[11] Zerbst, U., Bruno, G., Buffière, J.-Y., Wegener, T., Niendorf, T., Wu, T., Zhang, X., Kashaev, N., Meneghetti, G., Hrabe, N., Madia, M., Werner, T., Hilgenberg, K., Koukolíková, M., Procházka, R., Džugan, J., Möller, B., Beretta, S., Evans, A., Wagener, R., and Schnabel, K., "Damage Tolerant Design of Additively Manufactured Metallic Components Subjected to Cyclic Loading: State of the Art and Challenges," *Progress in Materials Science*, Vol. 121, 2021, p. 100786. https://doi.org/10.1016/j.pmatsci.2021.100786

[12] Fatemi, A., Molaei, R., Sharifimehr, S., Phan, N., and Shamsaei, N., "Multiaxial Fatigue Behavior of Wrought and Additive Manufactured Ti-6Al-4V Including Surface Finish Effect," *International Journal of Fatigue*, Vol. 100, 2017, pp. 347–366. https://doi.org/10.1016/j.ijfatigue.2017.03.044

[13] Sanaei, N., and Fatemi, A., "Defects in Additive Manufactured Metals and Their Effect on Fatigue Performance: A State-of-the-Art Review," *Progress in Materials Science*, Vol. 117, 2021, p. 100724. https://doi.org/10.1016/j.pmatsci.2020.100724

[14] King, W. E., Anderson, A. T., Ferencz, R. M., Hodge, N. E., Kamath, C., Khairallah, S. A., and Rubenchik, A. M., "Laser Powder Bed Fusion Additive Manufacturing of Metals; Physics, Computational, and Materials Challenges," *Applied Physics Reviews*, Vol. 2, No. 4, 2015, p. 041304. https://doi.org/10.1063/1.4937809

[15] Nelson, D. V., "Effects of Residual Stress on Fatigue Crack Propagation," *Residual Stress Effects in Fatigue*, Vol. ASTM STP 776-EB, 1982, pp. 172–194.

[16] Withers, P. J., and Bhadeshia, H., "Residual Stress. Part 2–Nature and Origins," *Materials science and technology*, Vol. 17, No. 4, 2001, pp. 366–375.

[17] Sunny, S., Mathews, R., Gleason, G., Malik, A., and Halley, J., “Effect of Metal Additive Manufacturing Residual Stress on Post-Process Machining-Induced Stress and Distortion,” *International Journal of Mechanical Sciences*, Vol. 202, 2021, p. 106534.

[18] Wang, Z., Denlinger, E., Michaleris, P., Stoica, A. D., Ma, D., and Beese, A. M., “Residual Stress Mapping in Inconel 625 Fabricated through Additive Manufacturing: Method for Neutron Diffraction Measurements to Validate Thermomechanical Model Predictions,” *Materials & Design*, Vol. 113, 2017, pp. 169–177. https://doi.org/10.1016/j.matdes.2016.10.003

[19] Fang, Z.-C., Wu, Z.-L., Huang, C.-G., and Wu, C.-W., “Review on Residual Stress in Selective Laser Melting Additive Manufacturing of Alloy Parts,” *Optics & Laser Technology*, Vol. 129, 2020, p. 106283. https://doi.org/10.1016/j.optlastec.2020.106283

[20] Chen, W., Xu, L., Han, Y., Zhao, L., and Jing, H., “Control of Residual Stress in Metal Additive Manufacturing by Low-Temperature Solid-State Phase Transformation: An Experimental and Numerical Study,” *Additive Manufacturing*, Vol. 42, 2021, p. 102016. https://doi.org/10.1016/j.addma.2021.102016

[21] Chen, W., Voisin, T., Zhang, Y., Forien, J.-B., Spadaccini, C. M., McDowell, D. L., Zhu, T., and Wang, Y. M., “Microscale Residual Stresses in Additively Manufactured Stainless Steel,” *Nature Communications*, Vol. 12, No. 1, 2021, p. 6780. https://doi.org/10.1038/s41467-021-27068-z

[22] Bandyopadhyay, R., Stopka, K. S., and Sangid, M. D., “Initializing Intragranular Residual Stresses within Statistically Equivalent Microstructures for Crystal Plasticity Simulations,” *Journal of the Mechanics and Physics of Solids*, 2023, p. 105529. https://doi.org/10.1016/j.jmps.2023.105529

[23] Gordon, J. V., Haden, C. V., Nied, H. F., Vinci, R. P., and Harlow, D. G., “Fatigue Crack Growth Anisotropy, Texture and Residual Stress in Austenitic Steel Made by Wire and Arc Additive Manufacturing,” *Materials Science and Engineering: A*, Vol. 724, 2018, pp. 431–438. https://doi.org/10.1016/j.msea.2018.03.075

[24] Simson, T., Emmel, A., Dwars, A., and Böhm, J., “Residual Stress Measurements on AISI 316L Samples Manufactured by Selective Laser Melting,” *Additive Manufacturing*, Vol. 17, 2017, pp. 183–189. https://doi.org/10.1016/j.addma.2017.07.007

[25] Withers, P. J., and Bhadeshia, H., “Residual Stress. Part 1–Measurement Techniques,” *Materials science and Technology*, Vol. 17, No. 4, 2001, pp. 355–365.

[26] Brown, D. W., Bernardin, J. D., Carpenter, J. S., Clausen, B., Spernjak, D., and Thompson, J. M., “Neutron Diffraction Measurements of Residual Stress in Additively Manufactured Stainless Steel,” *Materials Science and Engineering: A*, Vol. 678, 2016, pp. 291–298.

[27] Kartal, M. E., Kiwanuka, R., and Dunne, F. P. E., “Determination of Sub-Surface Stresses at Inclusions in Single Crystal Superalloy Using HR-EBSD, Crystal Plasticity and Inverse Eigenstrain Analysis,” *International Journal of Solids and Structures*, Vols. 67–68, 2015, pp. 27–39. https://doi.org/10.1016/j.ijsolstr.2015.02.023

[28] Kapoor, K., and Sangid, M. D., “Initializing Type-2 Residual Stresses in Crystal Plasticity Finite Element Simulations Utilizing High-Energy Diffraction Microscopy Data,” *Materials Science and Engineering: A*, Vol. 729, 2018, pp. 53–63. https://doi.org/10.1016/j.msea.2018.05.031

[29] Pokharel, R., and Lebensohn, R. A., “Instantiation of Crystal Plasticity Simulations for Micromechanical Modelling with Direct Input from Microstructural Data Collected at Light Sources,” *Scripta Materialia*, Vol. 132, 2017, pp. 73–77. https://doi.org/10.1016/j.scriptamat.2017.01.025

[30] Chatterjee, K., Venkataraman, A., Garbaciak, T., Rotella, J., Sangid, M. D., Beaudoin, A. J., Kenesei, P., Park, J. S., and Pilchak, A. L., “Study of Grain-Level Deformation and Residual Stresses in Ti-7Al under Combined Bending and Tension Using High Energy Diffraction Microscopy (HEDM),” *International Journal of Solids and Structures*, Vol. 94, 2016, pp. 35–49.

[31] Chan, K. S., and Lankford, J., “The Role of Microstructural Dissimilitude in Fatigue and Fracture of Small Cracks,” *Acta Metallurgica*, Vol. 36, No. 1, 1988, pp. 193–206. https://doi.org/10.1016/0001-6160(88)90038-7

[32] McDowell, D. L., “Basic Issues in the Mechanics of High Cycle Metal Fatigue,” *International Journal of Fracture*, Vol. 80, No. 2, 1996, pp. 103–145. https://doi.org/10.1007/BF00012666

[33] Pineau, A., McDowell, D. L., Busso, E. P., and Antolovich, S. D., “Failure of Metals II: Fatigue,” *Acta Materialia*, Vol. 107, 2016, pp. 484–507. https://doi.org/10.1016/j.actamat.2015.05.050

[34] Castelluccio, G. M., and McDowell, D. L., “Mesoscale Modeling of Microstructurally Small Fatigue Cracks in Metallic Polycrystals,” *Materials Science and Engineering: A*, Vol. 598, 2014, pp. 34–55. https://doi.org/10.1016/j.msea.2014.01.015

[35] Stopka, K. S., Yaghoobi, M., Allison, J. E., and McDowell, D. L., “Effects of Boundary Conditions on Microstructure-Sensitive Fatigue Crystal Plasticity Analysis,” *Integrating Materials and Manufacturing Innovation*, Vol. 10, No. 3, 2021, pp. 393–412. https://doi.org/10.1007/s40192-021-00219-2

[36] Yeratapally, S. R., Leser, P. E., Hochhalter, J. D., Leser, W. P., and Ruggles, T. J., “A Digital Twin Feasibility Study (Part I): Non-Deterministic Predictions of Fatigue Life in Aluminum Alloy 7075-T651 Using a Microstructure-Based Multi-Scale Model,” *Engineering Fracture Mechanics*, Vol. 228, 2020, p. 106888. https://doi.org/10.1016/j.engfracmech.2020.106888

[37] Przybyla, C. P., and McDowell, D. L., “Microstructure-Sensitive Extreme Value Probabilities for High Cycle Fatigue of Ni-Base Superalloy IN100,” *International Journal of Plasticity*, Vol. 26, No. 3, 2010, pp. 372–394. https://doi.org/10.1016/j.ijplas.2009.08.001

[38] Gu, T., Stopka, K. S., Xu, C., and McDowell, D. L., “Modeling the Statistical Distribution of Fatigue Crack Formation Lifetime in Large Volumes of Polycrystalline Microstructures,” *Acta Materialia*, Vol. 247, 2023, p. 118715. https://doi.org/10.1016/j.actamat.2023.118715

[39] Fatemi, A., and Socie, D. F., “A Critical Plane Approach to Multiaxial Fatigue Damage Including Out-of-phase Loading,” *Fatigue & Fracture of Engineering Materials & Structures*, Vol. 11, No. 3, 1988, pp. 149–165.

[40] Lass, E. A., Stoudt, M. R., Williams, M. E., Katz, M. B., Levine, L. E., Phan, T. Q., Gnaeupel-Herold, T. H., and Ng, D. S., “Formation of the Ni3Nb δ-Phase in Stress-Relieved Inconel 625 Produced via Laser Powder-Bed Fusion Additive Manufacturing,” *Metallurgical and Materials Transactions A*, Vol. 48, No. 11, 2017, pp. 5547–5558. https://doi.org/10.1007/s11661-017-4304-6

[41] Pagan, D. C., Phan, T. Q., Weaver, J. S., Benson, A. R., and Beaudoin, A. J., “Unsupervised Learning of Dislocation Motion,” *Acta Materialia*, Vol. 181, 2019, pp. 510–518. https://doi.org/10.1016/j.actamat.2019.10.011

[42] Nygren, K. E., Pagan, D. C., Bernier, J. V., and Miller, M. P., “An Algorithm for Resolving Intragranular Orientation Fields Using Coupled Far-Field and near-Field High Energy X-Ray Diffraction Microscopy,” *Materials Characterization*, Vol. 165, 2020, pp. 1–15. https://doi.org/10.1016/j.matchar.2020.110366

[43] Paul A. Shade, Basil Blank, Jay C. Schuren, Todd J. Turner, Peter Kenesei, Kurt Goetze, Robert M. Suter, Joel V. Bernier, Shiu Fai Li, Jonathan Lind, Ulrich Lienert, and Jonathan Almer, “A Rotational and Axial Motion System Load Frame Insert for in Situ High Energy X-Ray Studies,” *Review of Scientific Instruments*, Vol. 86, No. 9, 2015, pp. 1–8. https://doi.org/10.1063/1.4927855

[44] Poulsen, H. F., “Three-Dimensional X-Ray Diffraction Microscopy: Mapping Polycrystals and Their Dynamics,” Springer Science & Business Media, 2004.

[45] Malmelöv, A., Fisk, M., Lundbäck, A., and Lindgren, L.-E., “Mechanism Based Flow Stress Model for Alloy 625 and Alloy 718,” *Materials*, Vol. 13, No. 24, 2020, p. 5620.

[46] Joel V. Bernier, “HEXRD Software Package,” https://github.com/joelvbernier/hexrd, 2016.

[47] Strantza, M., Ganeriwala, R. K., Clausen, B., Phan, T. Q., Levine, L. E., Pagan, D. C., Ruff, J. P. C., King, W. E., Johnson, N. S., Martinez, R. M., Anghel, V., Rafailov, G., and Brown,

D. W., “Effect of the Scanning Strategy on the Formation of Residual Stresses in Additively Manufactured Ti-6Al-4V,” *Additive Manufacturing*, Vol. 45, 2021, p. 102003. https://doi.org/10.1016/j.addma.2021.102003

[48] Hurley, R. C., Herbold, E. B., and Pagan, D. C., “Characterization of the Crystal Structure, Kinematics, Stresses and Rotations in Angular Granular Quartz during Compaction,” *Journal of Applied Crystallography*, Vol. 51, No. 4, 2018, pp. 1021–1034. https://doi.org/10.1107/S1600576718006957

[49] Wang, Z., Stoica, A. D., Ma, D., and Beese, A. M., “Diffraction and Single-Crystal Elastic Constants of Inconel 625 at Room and Elevated Temperatures Determined by Neutron Diffraction,” *Materials Science and Engineering: A*, Vol. 674, 2016, pp. 406–412. https://doi.org/10.1016/j.msea.2016.08.010

[50] Quey, R., Dawson, P. R., and Barbe, F., “Large-Scale 3D Random Polycrystals for the Finite Element Method: Generation, Meshing and Remeshing,” *Computer Methods in Applied Mechanics and Engineering*, Vol. 200, No. 17, 2011, pp. 1729–1745. https://doi.org/10.1016/j.cma.2011.01.002

[51] Geuzaine, C., and Remacle, J.-F., “Gmsh: A 3-D Finite Element Mesh Generator with Built-in Pre-and Post-processing Facilities,” *International journal for numerical methods in engineering*, Vol. 79, No. 11, 2009, pp. 1309–1331.

[52] Warner, James E., Bomarito, Geoffrey F., Heber, Gerd, and Hochhalter, Jacob D., “Scalable Implementation of Finite Elements by NASA _ Implicit (ScIFEi),” NASA/TM-2016-219180.

[53] Kocks, U. F., “Laws for Work-Hardening and Low-Temperature Creep,” *Journal of Engineering Materials Technology*, Vol. 98, No. 1, 1976, pp. 76–85.

[54] Lee, E. H., “Elastic-Plastic Deformation at Finite Strains,” *Journal of Applied Mechanics*, Vol. 36, No. 1, 1969, pp. 1–6.

[55] Martin, N., Hor, A., Copin, E., Lours, P., and Ratsifandrihana, L., “Fatigue Properties of As-Built and Heat-Treated Inconel 625 Obtained by the Hybridization of Two Laser-Powder

Based Additive Processes," *International Journal of Fatigue*, Vol. 172, 2023, p. 107650. https://doi.org/10.1016/j.ijfatigue.2023.107650

[56] Gustafson, S., Ludwig, W., Shade, P., Naragani, D., Pagan, D., Cook, P., Yildirim, C., Detlefs, C., and Sangid, M. D., "Quantifying Microscale Drivers for Fatigue Failure via Coupled Synchrotron X-Ray Characterization and Simulations," *Nature Communications*, Vol. 11, No. 1, 2020, p. 3189. https://doi.org/10.1038/s41467-020-16894-2

[57] Wright, S. I., and Field, D. P., "Recent Studies of Local Texture and Its Influence on Failure," *Materials Science and Engineering: A*, Vol. 257, No. 1, 1998, pp. 165–170. https://doi.org/10.1016/s0921-5093(98)00835-1

[58] Tayon, W., Crooks, R., Domack, M., Wagner, J., and Elmustafa, A. A., "EBSD Study of Delamination Fracture in Al–Li Alloy 2090," *Experimental Mechanics*, Vol. 50, No. 1, 2010, pp. 135–143. https://doi.org/10.1007/s11340-008-9202-9

[59] Lucarini, S., and Segurado, J., "An Upscaling Approach for Micromechanics Based Fatigue: From RVEs to Specimens and Component Life Prediction," *International Journal of Fracture*, Vol. 223, No. 1, 2020, pp. 93–108. https://doi.org/10.1007/s10704-019-00406-5

[60] Zhang, J., Li, J., Wu, S., Zhang, W., Sun, J., and Qian, G., "High-Cycle and Very-High-Cycle Fatigue Lifetime Prediction of Additively Manufactured AlSi10Mg via Crystal Plasticity Finite Element Method," *International Journal of Fatigue*, Vol. 155, 2022, p. 106577. https://doi.org/10.1016/j.ijfatigue.2021.106577

[61] "Empirical Cumulative Distribution Function (ECDF)," 2023.

[62] Castelluccio, G. M., and McDowell, D. L., "Microstructure and Mesh Sensitivities of Mesoscale Surrogate Driving Force Measures for Transgranular Fatigue Cracks in Polycrystals," *Materials Science and Engineering: A*, Vol. 639, 2015, pp. 626–639. https://doi.org/10.1016/j.msea.2015.05.048

[63] Levieil, B., Doudard, C., Thevenet, D., Bridier, F., Ezanno, A., and Calloch, S., "Taking Residual Stresses into Account in Low-Cycle Fatigue Design Using the Adjustable

Localisation Operator Method," *International Journal of Fatigue*, Vol. 150, 2021, p. 106322. https://doi.org/10.1016/j.ijfatigue.2021.106322

[64] Stephens, R. I., Fatemi, A., Stephens, R. R., and Fuchs, H. O., "Metal Fatigue in Engineering," Wiley, 2000.

[65] Martucci, A., Marchese, G., Bassini, E., and Lombardi, M., "Effects of Stress-Relieving Temperature on Residual Stresses, Microstructure and Mechanical Behaviour of Inconel 625 Processed by PBF-LB/M," *Metals*, Vol. 13, No. 4, 2023, p. 796.

[66] Guo, C., Li, G., Li, S., Hu, X., Lu, H., Li, X., Xu, Z., Chen, Y., Li, Q., Lu, J., and Zhu, Q., "Additive Manufacturing of Ni-Based Superalloys: Residual Stress, Mechanisms of Crack Formation and Strategies for Crack Inhibition," *Nano Materials Science*, Vol. 5, No. 1, 2023, pp. 53–77. https://doi.org/10.1016/j.nanoms.2022.08.001